







In the format provided by the authors and unedited.

Interference of chiral Andreev edge states

Lingfei Zhao ¹✉, Ethan G. Arnault ¹, Alexey Bondarev¹, Andrew Seredinski¹, Trevyn F. Q. Larson¹, Anne W. Draelos¹, Hengming Li ², Kenji Watanabe ³, Takashi Taniguchi³, François Amet², Harold U. Baranger ¹ and Gleb Finkelstein ¹✉

¹Department of Physics, Duke University, Durham, NC, USA. ²Department of Physics and Astronomy, Appalachian State University, Boone, NC, USA.

³Advanced Materials Laboratory, NIMS, Tsukuba, Japan. ✉e-mail: lz117@duke.edu; gleb@phy.duke.edu

Supplementary Information for **Interference of chiral Andreev edge states**

Lingfei Zhao^{1*}, Ethan G. Arnault¹, Alexey Bondarev¹, Andrew Seredinski¹,
Trevyn F. Q. Larson¹, Anne W. Draelos¹, Hengming Li², Kenji Watanabe³,
Takashi Taniguchi³, François Amet², Harold U. Baranger¹ and Gleb Finkelstein^{1*}

¹Department of Physics, Duke University, Durham, NC 27708, USA

²Department of Physics and Astronomy, Appalachian State University, Boone, NC 28607, USA

³Advanced Materials Laboratory, NIMS, Tsukuba 305-0044, Japan

*Corresponding author. E-mail: lz117@duke.edu (L.Z.); gleb@phy.duke.edu (G.F.)

S1. Deviations of \tilde{R}_{xx} from the conventional longitudinal resistance

To rule out a bulk contribution to the non-zero \tilde{R}_{xx} on the quantum Hall (QH) plateaus, we have measured both the \tilde{R}_{xx} and the conventional longitudinal resistance R_{xx} using very similar setups. The inset of Fig. S1 shows the measurement configurations for R_{xx} (A) and for \tilde{R}_{xx} (B). In comparison with scheme B, the drain in scheme A is moved from the superconductor (SC) to the normal metal lead located further upstream. In this way, the bulk contribution to V_{xx} is almost the same because the voltage probes and the source remain unchanged, and the position of the drain moves only slightly. Fig. S1 shows that R_{xx} and \tilde{R}_{xx} nearly coincide away from the quantum Hall plateaus, where the contribution of the bulk states is most pronounced. They significantly differ in the plateau regions where R_{xx} is nearly zero. We conclude that the non-zero \tilde{R}_{xx} on the plateaus is the result of the influence of superconductor on the quantum Hall edge states which we recognize as the CAES.

To further stress the point that the non-trivial \tilde{R}_{xx} originates at the grounded superconduct-

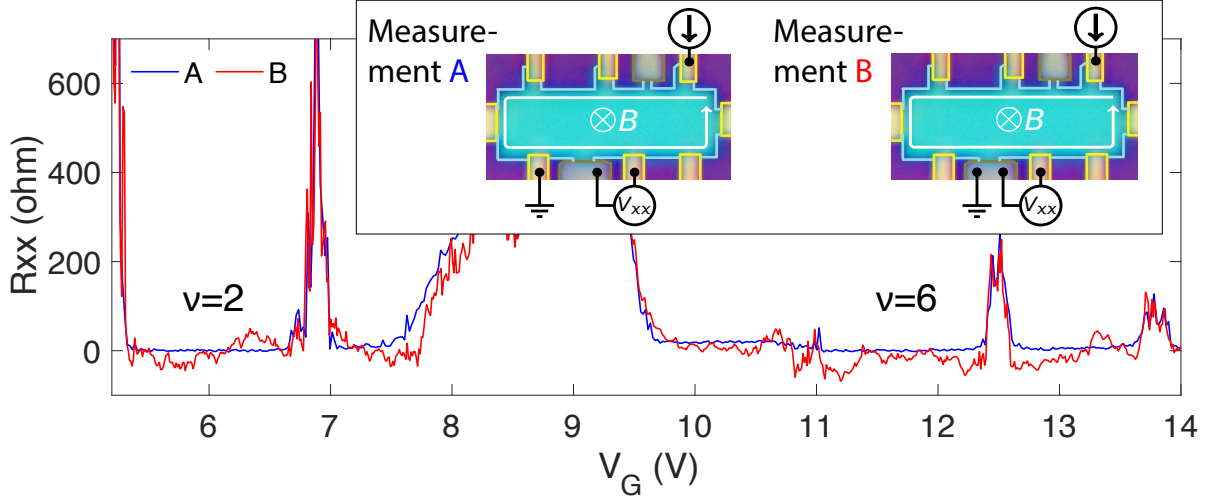


Fig. S1: Longitudinal resistance measured at $B = 4$ T as a function of gate voltage V_G in two configurations: A (blue) and B (red). Configuration B is identical to the one used elsewhere in the text; configuration A is conventional for quantum Hall measurements: the voltage is measured between two floating contacts. Note that in both cases the source and the voltage probes are the same, but in A the drain is moved further to the left (upstream) from the superconducting contact that was grounded in B. Configuration A results in vanishing R_{xx} , as expected.

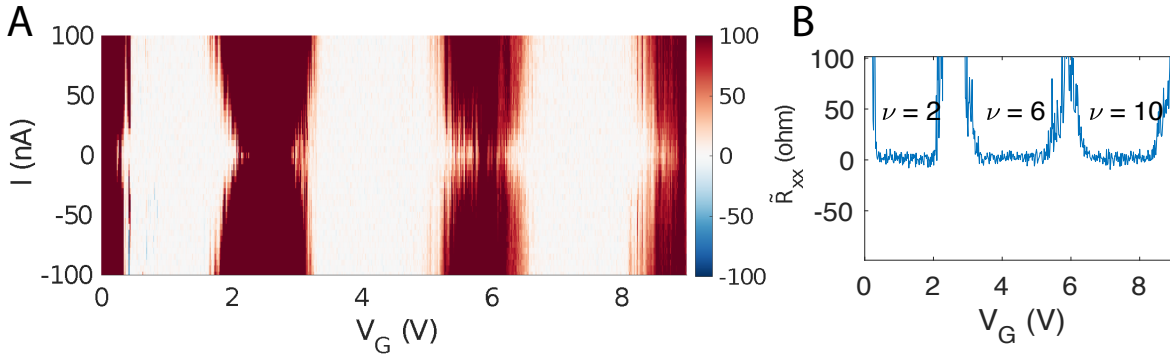


Fig. S2: \tilde{R}_{xx} measured downstream from a normal contact at 2 Tesla. The white regions (panel A) of zero \tilde{R}_{xx} correspond to filling factors 2, 6 and 10. The zero-bias cut is presented in panel B.

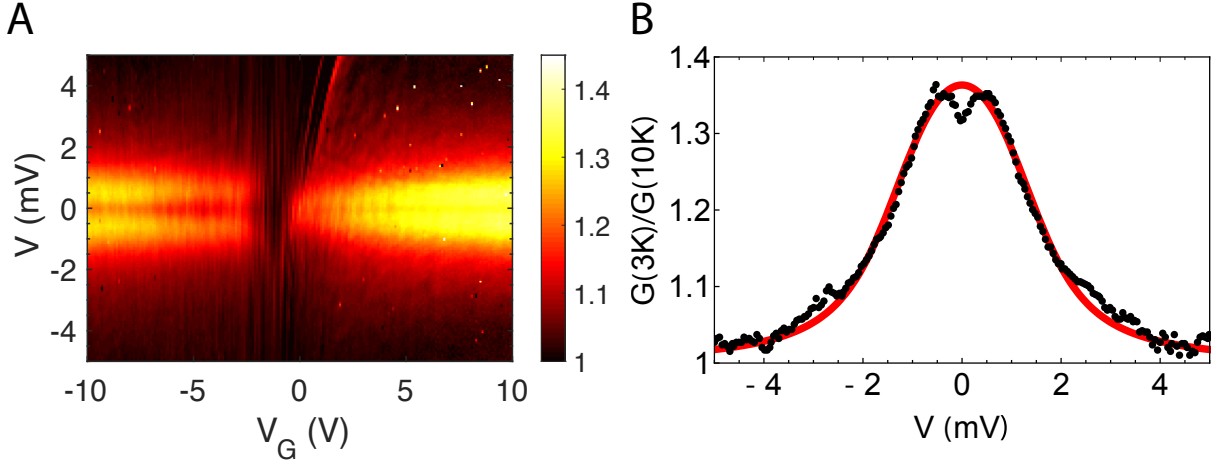


Fig. S3: Differential conductance of the graphene-MoRe interface measured at $B = 0$ and $T = 3$ K, normalized by the high temperature conductance, $G(V, 3K)/G(V, 10K)$. (A) Normalized conductance plotted versus bias voltage V and gate voltage V_G . Low-bias conductance enhancement is observed at low temperatures through most of the gate voltage range. (B) Normalized conductance versus bias at $V_G = 10$ V. The red curve is calculated using the modified Blonder-Tinkham-Klapwijk theory [1] by taking the superconducting gap $\Delta = 1.3$ meV, energy broadening $\Gamma = 0.5\Delta$, barrier parameter $Z = 0$ and temperature $T = 3$ K. (Here, we use a different sample than the one presented in the main text; however, the contacts are fabricated following the same procedure.)

ing interface, we measure a similar sample with normal contacts. Fig. S2 shows \tilde{R}_{xx} measured for the normal contact with the interface length of $1 \mu\text{m}$, comparable to the graphene-superconductor interface length studied in the paper. No discernable deviations from zero resistance are observed in this case.

To rule out effects from non-transparent interfaces, we have studied a similar device (graphene with a MoRe contact and normal contacts). The differential conductance of the interface is measured in a properly filtered 3 K cryostat and normalized by the 10 K (above the $T_c \approx 9$ K) data. Fig. S3 plots the normalized differential conductance at zero magnetic field as a function of the bias voltage and gate voltage. Enhanced conductance inside the superconducting gap is universally observed away from the Dirac point ($V_G = -1.3$ V). In the well n-doped region ($V_G > 5$ V), the enhancement factor is above 1.3 suggesting a highly transparent contact (note that the

enhancement should be even higher at lower temperatures). We fit the normalized differential conductance at $V_G = 10$ V to the modified Blonder-Tinkham-Klapwijk model [1] (see panel B) and find the superconducting gap $\Delta = 1.3$ meV, energy broadening $\Gamma = 0.5\Delta$ and barrier parameter $Z = 0$. These findings also agree with a transparent graphene-MoRe interface. (A small barrier is likely present, evidenced by a small dip at zero bias, but the fitting cannot reliably determine its value.)

S2. Toy model of the interference of chiral Andreev edge states

For a spinless edge state, the s-wave superconducting proximity effect can be described by the Bogoliubov-de Gennes Hamiltonian in the basis of $\{|e\rangle, |h\rangle\}$ [2]. Its particle-hole symmetry ensures that the two eigenstates at zero energy can be written as [3]

$$\begin{aligned} |\psi_1\rangle &= \alpha |e\rangle + \beta |h\rangle \\ |\psi_2\rangle &= \beta^* |e\rangle - \alpha^* |h\rangle, \end{aligned} \tag{S1}$$

where $|\alpha|^2 + |\beta|^2 = 1$. An incoming electron $|e\rangle = \alpha^* |\psi_1\rangle + \beta |\psi_2\rangle$ propagates through the proximity region as

$$\begin{aligned} |\phi\rangle &= \alpha^* e^{ik_1 L} |\psi_1\rangle + \beta e^{ik_2 L} |\psi_2\rangle \\ &= (|\alpha|^2 e^{ik_1 L} + |\beta|^2 e^{ik_2 L}) |e\rangle + (e^{ik_1 L} - e^{ik_2 L}) \alpha^* \beta |h\rangle, \end{aligned} \tag{S2}$$

where k_1, k_2 are the wavevectors of the two modes and L is the propagation length. The probability of converting an electron into a hole is then $P_h = 4|\alpha|^2|\beta|^2 \sin^2(\delta k L/2)$, where $\delta k = k_1 - k_2$, so that $\delta k L$ is the acquired phase difference between the two modes. Thus the charge coming out of the CAES is

$$q = e(P_e - P_h) = e(1 - 2P_h) = e(1 - 8|\alpha|^2|\beta|^2 \sin^2(\delta k L/2)). \tag{S3}$$

Averaging over the phase difference, we find

$$\bar{q} = e(1 - 4|\alpha|^2|\beta|^2). \tag{S4}$$

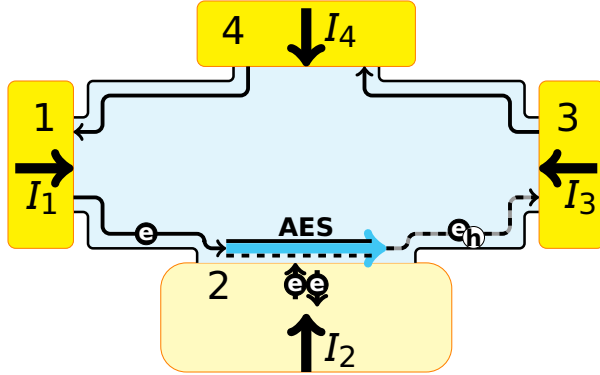


Fig. S4: Sketch of the four-terminal transport measurement, in which the bottom contact 2 is superconducting and the others are normal. An electron injected into the CAES (bottom left) comes out as a hole or electron (bottom right) with a probability P_h or P_e .

Notice that the average result is neutral when the two eigenstates are neutral ($|\alpha|^2 = |\beta|^2 = 1/2$): when the interface modes are neutral electron-hole hybrids, an incoming electron is equally likely to produce an outgoing hole as an outgoing electron.

In the $\nu = 2$ quantum Hall state that is the focus of this paper, the spins of the electrons are not polarized, and so there are two possible spin states for the electrons and two for the holes. Thus, there are four eigenstates of the Bogoliubov-de Gennes Hamiltonian at zero energy, which are pairwise charge conjugate to each other. For the argument above, we have assumed that both $|\psi_1\rangle$ and $|\psi_2\rangle$ are spin degenerate. In a more sophisticated analysis this does not have to be the case.

S3. Landauer-Büttiker picture

As shown in Fig. S4, a two-dimensional electron gas device with ν chiral channels is contacted with four metal leads. The bottom lead is a grounded superconductor and the other three are normal metal. We calculate the zero-bias Hall conductance G_{xy} and superconductor downstream resistance \tilde{R}_{xx} at zero temperature using the Landauer-Büttiker formula [4] assuming (i) no electron can transfer into the superconductor without forming a Cooper pair and (ii) an

electron injected into the CAES comes out as a hole (or electron) with a probability P_h (or P_e).

The relation between the current in the leads I_i and the voltage on them V_j is

$$\begin{pmatrix} I_1 \\ I_2 \\ I_3 \\ I_4 \end{pmatrix} = \nu \frac{e^2}{h} \begin{pmatrix} 1 & 0 & 0 & -1 \\ -1 + (P_e - P_h) & 1 - (P_e - P_h) & 0 & 0 \\ -(P_e - P_h) & -1 + (P_e - P_h) & 1 & 0 \\ 0 & 0 & -1 & 1 \end{pmatrix} \begin{pmatrix} V_1 \\ V_2 \\ V_3 \\ V_4 \end{pmatrix} = \begin{pmatrix} 0 \\ -I \\ 0 \\ I \end{pmatrix}. \quad (\text{S5})$$

Deriving the conductance matrix in the superconducting case requires extra care due to the Andreev processes. Here we derive the individual lines in Eq. S5 following reference [5]. The net currents flowing through contacts 1 and 4 are unaffected by superconductivity. The currents affected by Andreev reflections are I_2 and I_3 . Let us refer all the voltages with respect to the grounded superconducting contact 2. I_2 is the current of Cooper pairs flowing out of the contact 2. It can be calculated as a current of electrons coming from contact 1, Andreev reflected with a probability P_h :

$$I_2 = -\frac{\nu e^2}{h} (V_1 - V_2) 2P_h \quad (\text{S6})$$

The factor of 2 indicates that for each Andreev reflection of an electron to a hole, a Cooper pair is added to the superconducting contact. Rewriting $2P_h$ in the symmetric form $1 - P_e + P_h$ gives the second line in Eq. S5.

I_3 consists of the trivial current flowing downstream from contact 3, minus the non-trivial current flowing to contact 3 from the upstream direction. The latter term is calculated from the probability of an electron from contact 1 to flow past contact 2 as an electron or to turn into a hole: $\frac{\nu e^2}{h} (P_e - P_h)(V_1 - V_2)$. (Alternatively, one can think of this term as the difference of currents flowing from contact 1 and the current absorbed by contact 2.) Overall,

$$I_3 = \frac{\nu e^2}{h} ((V_3 - V_2) - (P_e - P_h)(V_1 - V_2)) \quad (\text{S7})$$

We can now check the consistency of the resulting matrix. Current conservation dictates that the sum of the elements in a column must be equal to zero. The sum of the elements in

every row should also be zero: if we apply a uniform change of the chemical potential to all contacts, the currents through any contact should remain the same. The conductance matrix indeed satisfies both sets of conditions.

Solving Eq. S5, we find the Hall conductance G_{xy} and superconductor downstream resistance \tilde{R}_{xx}

$$\begin{aligned} G_{xy} &= \frac{I}{V_1 - V_3} = \nu \frac{e^2}{h} \\ \tilde{R}_{xx} &= \frac{V_3 - V_2}{I} = \frac{P_e - P_h}{1 - (P_e - P_h)} G_{xy}^{-1}. \end{aligned} \quad (\text{S8})$$

The CAES may be absorbed by the superconductor as quasi-particle excitations, reducing both P_e and P_h . We introduce a phenomenological “survival probability” $P_{\text{surv.}}$ to describe the fraction of the particles reaching the end of the interface. We then multiply $P_e - P_h$ by $P_{\text{surv.}}$, and the superconductor downstream longitudinal resistance \tilde{R}_{xx} becomes

$$\tilde{R}_{xx} = \frac{V_3 - V_2}{I} = \frac{(P_e - P_h)P_{\text{surv.}}}{1 - (P_e - P_h)P_{\text{surv.}}} G_{xy}^{-1}. \quad (\text{S9})$$

Note that since in the experiment $\tilde{R}_{xx} \ll h/e^2$, the survival probability has to be smaller than 1. Under this condition, $\tilde{R}_{xx} \approx (P_e - P_h)P_{\text{surv.}}G_{xy}^{-1}$.

S4. Stochastic switching behavior

As discussed in the main text, the downstream resistance \tilde{R}_{xx} measured on top of well quantized G_{xy} plateaus shows stochastic switching behavior. Fig. S5 presents the details of this switching by zooming into a small region of Fig. 2B. Zero-bias $G_{xy}(V_G)$ and $\tilde{R}_{xx}(V_G)$ are plotted in a field range of 3 to 3.1 T on top of the $\nu = 2$ plateau. Clearly, \tilde{R}_{xx} exhibits switching behavior (vertical lines) while G_{xy} remains smooth, as seen by the continuity of the inclined mesoscopic features at the transition between the plateaus. G_{xy} uses the same normal contacts (**a** and **d** in Fig. 1A) and probes the same region of the sample as \tilde{R}_{xx} ; the only difference is that the

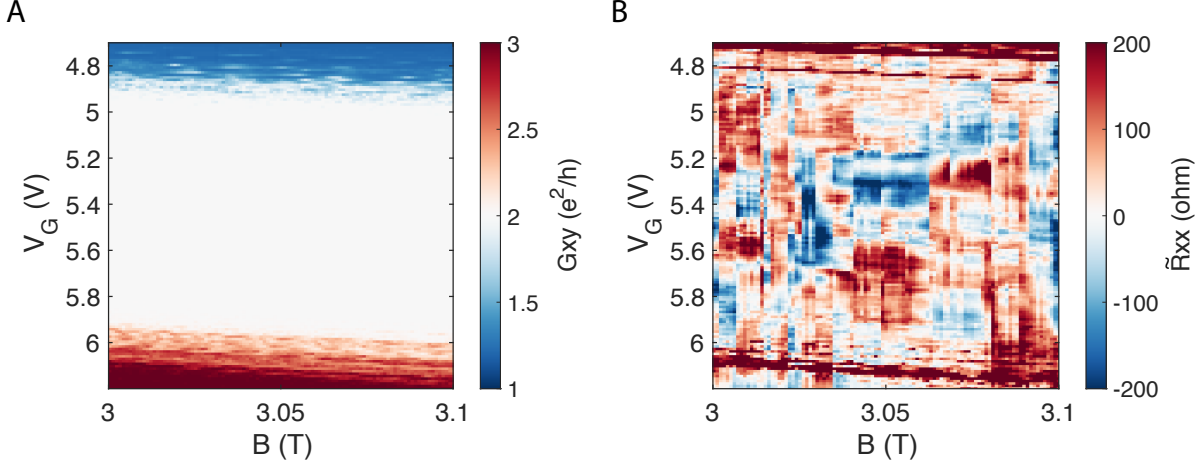


Fig. S5: Detailed maps of zero-bias G_{xy} (A) and \tilde{R}_{xx} (B) simultaneously measured while ramping the field down from 3.1 T to 3 T.

measurement of \tilde{R}_{xx} involves the voltage on the superconducting contact c . We thus attribute the switching to the rearrangement of vortices in that contact.

To support this argument, we measure \tilde{R}_{xx} as a function of bias at a fixed gate voltage $V_G = 5.67$ V while sweeping the magnetic field back and forth near 3 T. As shown in the first quadrant of Fig. S6, we start by sweeping the magnetic field from 3.02 T to 3 T. During this process, \tilde{R}_{xx} switches from a dip at zero bias to a peak and then back to a dip around 3.013 T. Then we sweep the magnetic field from 3.02 T back to 3 T (the second quadrant), during which \tilde{R}_{xx} directly switches from a zero-bias dip to another dip pattern around 3.01 T. At the end of the cycle, \tilde{R}_{xx} goes back to the initial state at 3.02 T. The remaining two plots show successive sweeps down and up, which produce very similar patterns.

The arrangement of vortices in the superconductor near the interface can strongly influence the phases of the interface modes. This is particularly clear in the semiclassical picture where a particle skipping along the edge picks up a phase from the superconductor upon each Andreev reflection. These phases are determined by the arrangement of vortices. In the quantum picture, such as $\nu = 2$ studied here, the beating between the CAES changes due to these phases. There-

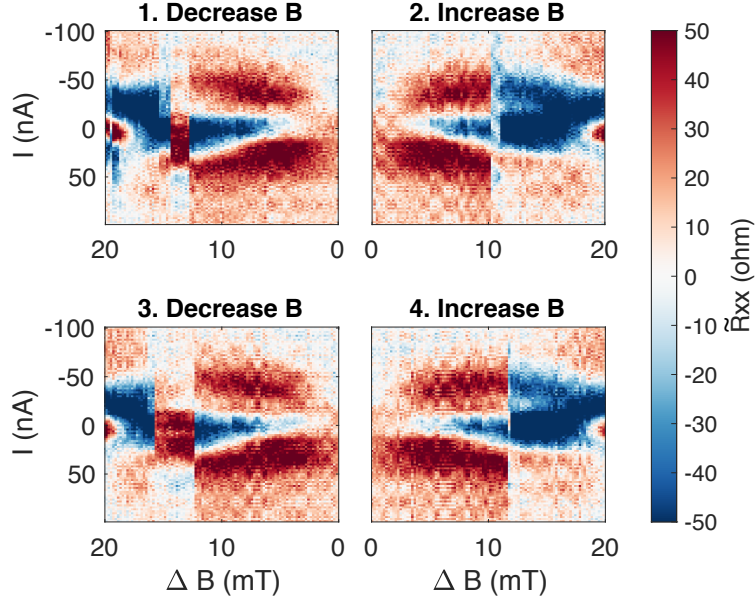


Fig. S6: The downstream resistance \tilde{R}_{xx} measured at $V_G = 5.67$ V as a function of the bias current and ΔB , the deviation of the magnetic field from 3 T. The 4 panels correspond to successive field sweeps from 3.02 T to 3 T and up again, repeated twice.

fore, the data presented in Fig. S6 can be interpreted as follows. As the magnetic field decreases from about 3.015 T to 3.01 T, two vortices appear to be removed one by one, generating a dip-peak-dip switching feature in \tilde{R}_{xx} . The two vortices are apparently added back at the same time when we increase the magnetic field (panel 2) so that only one switch is observed at $B \approx 3.01$ T.

S5. More data of the interference of CAES

To complement Fig. 3, in Fig. S7 we show the bias-gate oscillations of \tilde{R}_{xx} on the $\nu = 6$ plateau at $B = 3$ T. By converting the current I to voltage I/G_{xy} , we see that \tilde{R}_{xx} of both $\nu = 2$ and 6 oscillates only up to a voltage bias about 1 mV (see Fig. S8). Note that this range is approximately equal to the superconducting gap of MoRe ($\Delta_0 \approx 1.3$ meV). As this is the only energy scale at this order of magnitude in this system, the measurement further confirms that

the underlying physics is due to superconducting correlations.

This observation supports our interpretation in terms of interference among CAES. To further rule out any alternative explanations of these oscillations, we plot the bias-gate map of \tilde{R}_{xx} on $\nu = 2$ and 6 at various temperatures in Fig. S9. The oscillation patterns gradually die off with rising temperature, leaving zero resistance independent of bias and gate voltage at 2.6 K. We also note that the bias-dependent oscillations for $\nu = 6$ are more irregular (see e.g. Fig. S7B) than those of $\nu = 2$, suggesting the beating of multiple modes when the number of CAES is large.

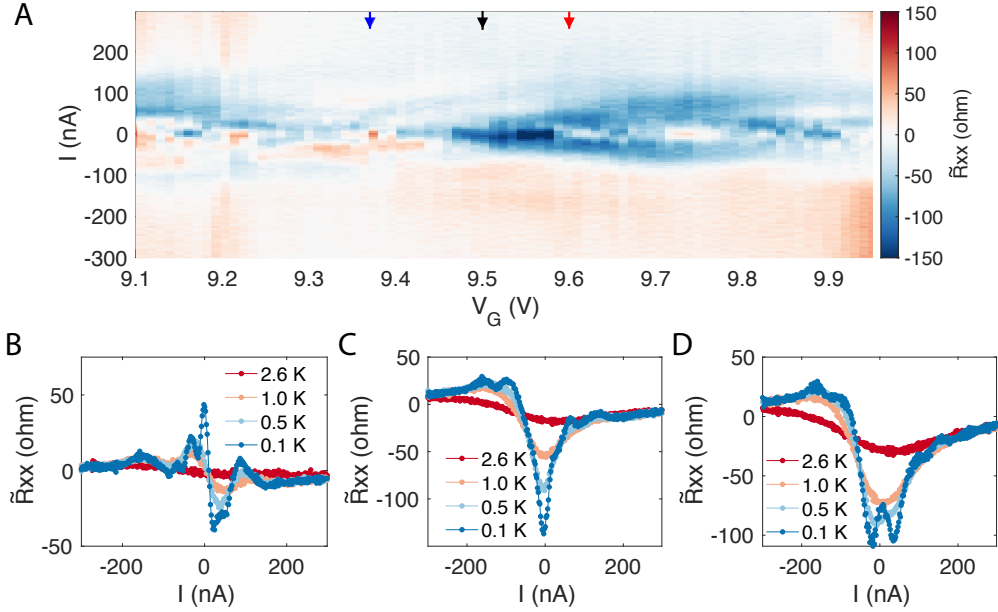


Fig. S7: (A) The superconductor downstream longitudinal resistance \tilde{R}_{xx} plotted versus the DC bias current I_{bias} and gate voltage V_G on the $\nu = 6$ plateau at $B = 3$ T. Gate-dependent oscillations centered at zero-bias are observed inside the well-quantized region, indicating interference of the CAES. (B-D) Bias-dependent oscillations of \tilde{R}_{xx} at the gate voltages $V_G = 9.37$ (B), 9.50 (C), 9.60 (D) V marked by the arrows in (A).

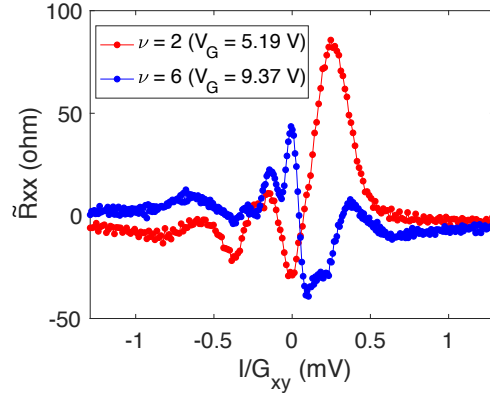


Fig. S8: Comparison of \tilde{R}_{xx} plotted vs. bias voltage at two filling factors $\nu = 2$ and 6.

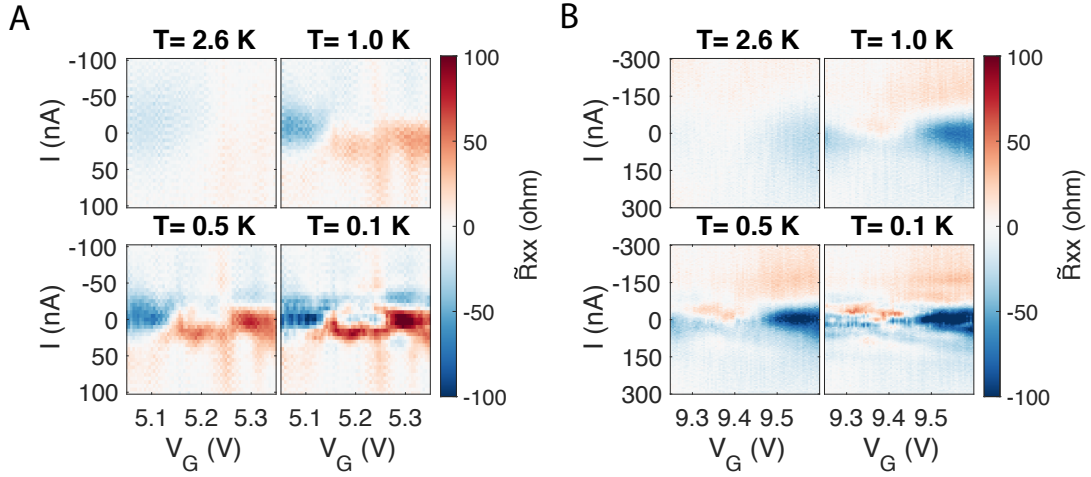


Fig. S9: Temperature dependence of the bias-gate maps of \tilde{R}_{xx} at $B = 3$ T on the plateaus (A) $\nu = 2$ and (B) $\nu = 6$.

S6. Tight-binding calculation

In our numerical calculation, we consider an armchair graphene nanoribbon in contact with a superconductor, which is modeled as a square lattice with a superconducting gap. We avoid using a honeycomb lattice to represent the superconductor. In our earlier attempts to simulate the superconductor using the graphene lattice, the valley symmetry at the NS interface resulted in a pair of degenerate CAES. In this case the Andreev reflection probability is simply determined by the valley isospin of the edge states on the two sides of the superconducting contact [6]. We emphasize that simulations using the square lattice for the superconductor are expected to represent a generic situation for a graphene-superconductor interface that does not have the valley symmetry. We have obtained similar results with both armchair and zigzag graphene nanoribbons. The graphene region is penetrated by a perpendicular magnetic field. We consider two basic geometries: 1) We calculate the transport properties using the setup shown in the left panel of Fig. S10 with the lattice structure sketched in the inset. The square lattice of superconductor is stitched to the armchair edge of graphene lattice. The length of this interface is $301.5 a$, where a is the lattice parameter of graphene as indicated in the inset. Leads are attached to the left and right sides of the graphene region for calculating the transport properties. 2) To calculate properties in momentum space, such as the dispersion relations, we extend the interface shown in Fig. S10 infinitely in the x direction.

The graphene is modeled using the simple π -orbital nearest neighbor tight-binding model on a honeycomb lattice [4]. For simplicity, the model considered here is spinless. As a result, there is only one quantum Hall edge channel for the filling factor $\nu = 2$ studied here. The hopping energy in the graphene region and across the interface is set to be $t_G = 3.033$ eV. The hopping energy in the superconductor region is $t_G/2$. The magnetic field is incorporated with the standard Peierls substitution in a Landau gauge. The parameters are chosen such that the flux through a unit cell of the lattice is much less than a flux quantum, $\Phi/\Phi_0 \ll 1$, even

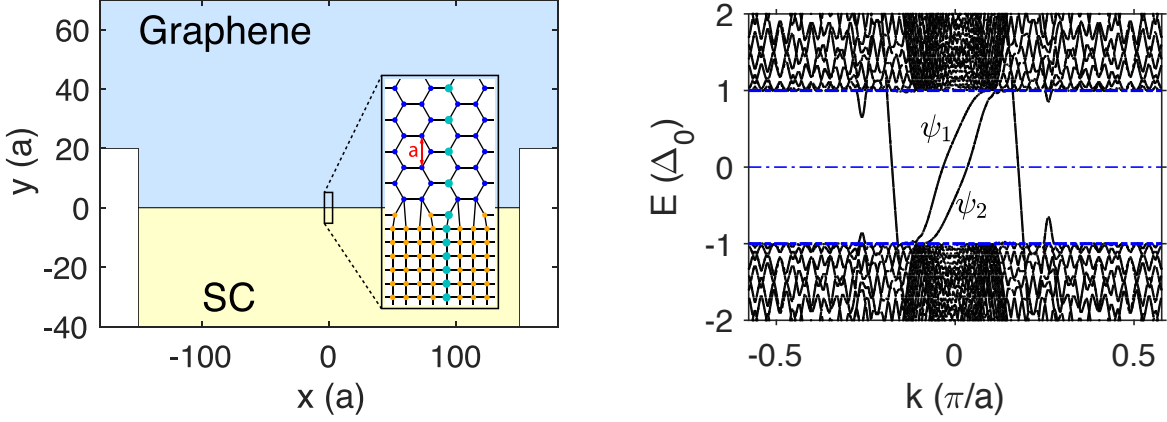


Fig. S10: Schematic of the geometry (left panel): The graphene lattice (blue) is stitched to the superconductor lattice (yellow) as illustrated in the inset. The lattice parameter of graphene, a , is marked red. The electron and hole density on the cyan atoms are plotted in Fig. S11 for CAES ψ_1 and ψ_2 . Dispersion relation (right panel). Close to zero chemical potential ($E = 0$), modes with a positive slope move along the quantum Hall-superconductor interface while those with a negative slope are located at the quantum Hall-vacuum edge and move in the opposite direction. The δk between ψ_1 and ψ_2 gives rise to beating of the electron-hole hybridization, thus causing the resistance fluctuations seen experimentally. [$\mu_G = 0.145 t_G$, $B = 0.0095 h/ea^2$.]

in the lowest Landau level (LLL, $\nu = 2$). The density of electrons is typically different in the quantum Hall and superconductor regions, corresponding to a difference in the Fermi energy which we use as a crude model of the difference in work functions in the experimental system. The Fermi energy in the graphene region, μ_G , is defined relative to the Dirac point, while in the superconductor region, μ_{SC} is defined relative to the band minimum. We set $\mu_{SC} = \mu_G + t_G$ to align the chemical potentials of the two regions.

Superconductivity is simulated by using an electron and hole orbital on each site, coupled by a gap energy $\Delta_0 = 0.03 t_G$. This is not, of course, an exact representation of Bardeen-Cooper-Schrieffer theory, but it does correctly mimic the effect of superconductivity on adjacent normal regions. As the transport quantities in which we are interested can be calculated entirely from the normal state properties, this suffices for our purposes. The Bogoliubov-de Gennes equation [7] is then solved assuming abrupt magnetic field and gap profiles, $B(y) = BH(y)$

and $\Delta(y) = \Delta_0 H(-y)$, where $H(y)$ is the Heaviside step function.

For non-interacting electrons, methods for calculating the interface modes, scattering wavefunctions, and transport are well known [8, 9]. We use the package Kwant [10] to calculate the S -matrix, dispersion relations, and wavefunctions of the CAES along the quantum Hall-superconductor interface. From the S -matrix, we obtain the probability of an electron transmits through the CAES region as an electron versus a hole, $P_e - P_h$. This quantity is related to the experimentally measured differential resistance \tilde{R}_{xx} by the Landauer-Büttiker formula obtained in section S3.

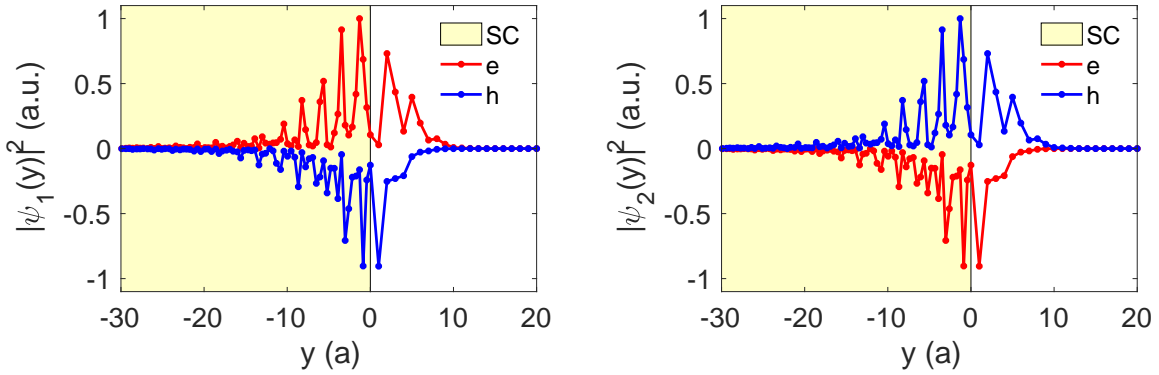


Fig. S11: Wavefunctions of the interface modes at $E = 0$ for $\nu = 2$: electron and hole density (plotted with opposite sign for clarity) for the two CAES ψ_1 (left) and ψ_2 (right). Note that the electron and hole wavefunction in each mode are not the same and that the two modes are conjugates of each other. [$\mu_G = 0.145 t_G$, $B = 0.0095 h/ea^2$.]

We now turn to the results of our calculation. The dispersion relation of the interface modes, $E(k)$ where k is the wavevector along the interface, is a key factor in explaining the experimentally observed oscillations. Thus, we show the dispersion relation for $\nu = 2$ in the right panel of Fig. S10; for a zoom on the key interface modes, see Fig. 3E of the main text. The edge modes that are propagating at the chemical potential ($E = 0$) are clearly singled out—for $\nu = 2$, there are two CAES along the quantum Hall-superconductor interface (positive slope) and two modes

along the vacuum interface (negative slope). Spin degeneracy leads to a further doubling of the number of modes. Note that the group velocity ($dE/\hbar dk$) of the CAES is lower than that of the modes along the vacuum edge of graphene. Because the wavevectors for the two CAES at the chemical potential are different, a superposition of such modes will undergo beating in position space.

The electron-hole hybrid nature of CAES is immediately seen by looking at the corresponding transverse wavefunctions. The two CAES at the chemical potential are shown in Fig. S11. Note that the electron density of one mode is the same as the hole density of the other, as expected for a pair of modes that are charge conjugate. In a given wavefunction, electron and hole weights are approximately equal: in the case shown, the ratio of the integrated electron density to that of the hole is about 1.14. However, as the electron and hole wavefunction of a given mode are certainly not the same, these modes are not charge neutral locally.

In the calculation, a particularly striking illustration of the beating between the CAES is obtained by plotting the electron and hole probability densities for a single scattering wave, as shown in Fig. 1D of the main text. In the case shown, an incoming electron (left vacuum edge) oscillates between electron and hole along the interface and then exits as a hole (right vacuum edge). The parameters used are $\mu_G = 0.145 t_G$, $B = 0.0095 h/ea^2$ and $E = 0$.

Sensitivity of the observed transport quantities to *gate voltage* is one of the main experimental signatures of interference effects among the chiral Andreev edge states. In the calculation, changing the gate voltage corresponds to changing the Fermi energy. The Fermi energy is changed uniformly throughout the system, in both the quantum Hall and superconductor portions. This has relatively small effect on the largely filled band of the superconductor, and mostly affects the graphene. Fig. S12 shows calculation results for conversion at the quantum Hall-superconductor interface: the difference in reflection probability as an electron versus a hole would produce an oscillating \tilde{R}_{xx} as per Eq. (S8). On the right panel, the variation of the

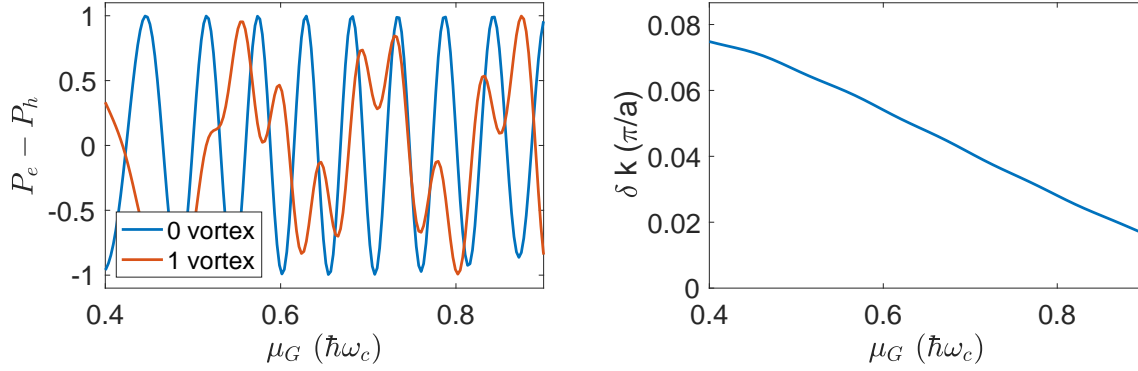


Fig. S12: The probability difference $P_e - P_h$, as a function of the Fermi energy in graphene. When a twist in the phase of the superconducting order parameter $\Delta(x)$ is added to simulate the effect of a vortex in the superconductor, the transport changes drastically (blue for constant Δ , red for twist). The difference in wavevector of the two modes is shown in the right panel. [$E = 0$, $B = 0.0095 h/ea^2$. At this field the cyclotron energy $\hbar\omega_c = 0.3 t_G$.]

wavevector difference, $\delta k(\mu_G)$, that underlies the modulation is shown.

Changing the *magnetic field* changes the phase of the wavefunctions and so modulates the beating. Fig. S13 shows the resulting change in the transmission probabilities P_e and P_h as a function of the magnetic field. The oscillation seen is the result of the change in δk , the difference between the wavevectors of the two hybrid modes, vs. B , as shown in the right panel.

To address the *sharp switching* seen experimentally as a function of magnetic field, as in Fig. S5&S6 and Fig. 2 of the main text, we perform calculations with a complex gap Δ in which the phase varies along the quantum Hall-superconductor interface. We insert one vortex, which we crudely simulate by a twist in the phase by π over a small distance. Fig. S12 shows that this leads to a very different dependence of the electron/hole transmission probability on gate voltage, consistent with the experimental observations.

Variation of the transport properties with *bias* comes from the energy dependence of δk as

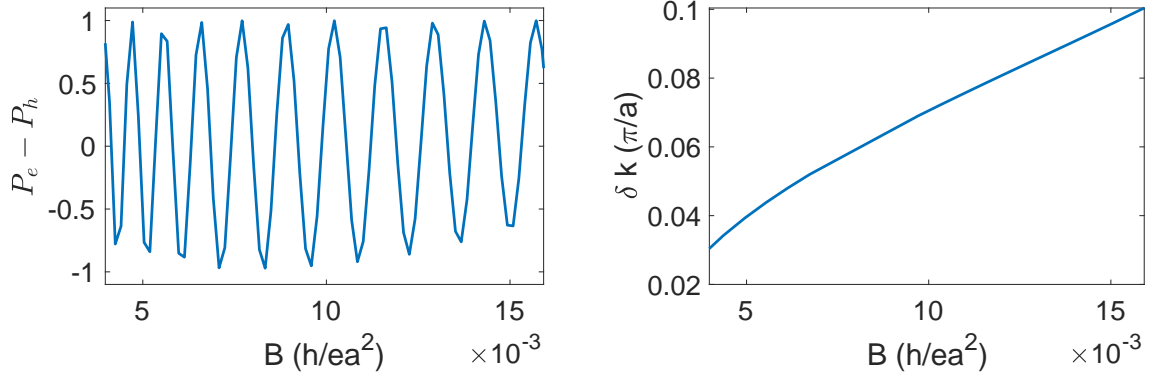


Fig. S13: The probability that outgoing particle is an electron, P_e , minus that of a hole, P_h , as a function of the magnetic field B . These oscillations result from the variation of the wavevector difference between the two CAES, δk , as shown in the right panel. [$\mu_G = 0.145 t_G$.]

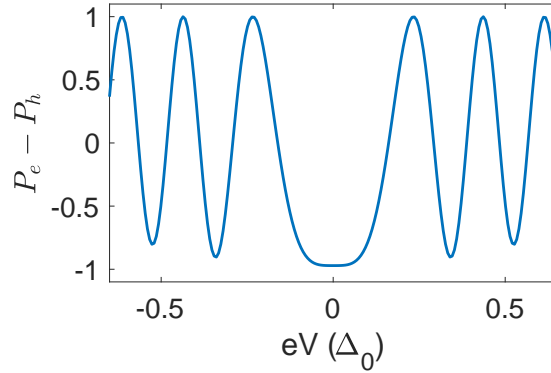


Fig. S14: The probability difference $P_e - P_h$, as a function of the applied bias $E = eV$. Energy dependence of the reflection probabilities makes the differential resistance nonlinear, as seen experimentally. [$\mu_G = 0.145 t_G$, $B = 0.0095 h/ea^2$.]

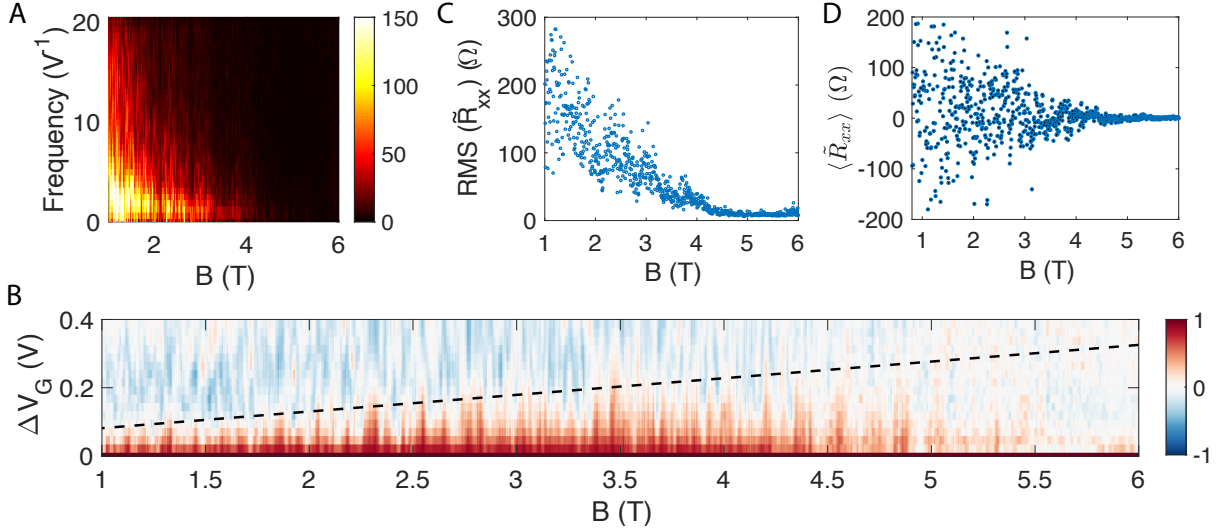


Fig. S15: Statistical Analysis of $\tilde{R}_{xx}(V_G)$ on the $\nu = 2$ plateau. The data used here are taken from Fig. 2B. **(A)** $\left|FFT\left[\tilde{R}_{xx}(V_G)\right]\right|$ as a function of the magnetic field. The map is smoothed in the B direction by a moving average window of 20 mT. **(B)** The normalized autocorrelation function of $\tilde{R}_{xx}(V_G)$ as a function of magnetic field. The data are smoothed in the B direction by a moving average window of 20 mT. The dashed line shows $1/5$ of the plateau width. **(C)** The root-mean-square (RMS) of \tilde{R}_{xx} as a function of B. **(D)** The average value of \tilde{R}_{xx} as a function of B.

one deviates from the chemical potential. Indeed, increasing the applied bias implies injecting higher energy electrons at the quantum Hall-superconductor interface. Introducing energy dependent reflection probabilities, $P_e(E)$ and $P_h(E)$, we show the probability of an incoming electron to exit the interface region as an electron versus a hole in Fig. S14. The energy dependence of the scattering produces oscillations in the differential transport similar to those observed experimentally.

S7. Statistics of \tilde{R}_{xx}

We present the amplitude of the single-sided Fourier spectra of the downstream resistance ($\nu = 2$), $\left|FFT\left[\tilde{R}_{xx}(V_G)\right]\right|$, as a function of magnetic field in Fig. S15A. Unfortunately, the experimental signal oscillates only a few times over the width of the plateau (see e.g. Fig. 1C).

As a result, the most important information appears at the lowest frequencies, making it challenging to distinguish the relevant information from FFT window effects.

The dominant frequency of the oscillation is about 2 to 3 periods per volt, and the peak merges with a very broad background. This background corresponds to the random fluctuations of the signal, which are most likely explained by the disordered nature of the interface. The FFT amplitude at all frequency decreases with temperature or magnetic field, which indicates that all these components share the same origin.

The autocorrelation of the signal (related to the Fourier spectrum) appears to be more informative. In Fig. S15B we first present the normalized autocorrelation of $\tilde{R}_{xx}(V_G)$ for $\nu = 2$ at various magnetic fields, extracted from Fig. 2B. The autocorrelation is non-trivial for $1T < B < 4T$, and gradually turns into noise above 5T. It appears that the region of positive autocorrelation grows proportionally with the width of the plateau. (The dashed line in Fig. S15B shows one-fifth of the plateau width, which agrees well with the region of positive autocorrelation.) In addition to the Fourier spectrum, this observation suggests that \tilde{R}_{xx} on average has 2 to 3 major oscillations on the plateau, independent of the magnetic field. Finally, we calculate the standard deviation of \tilde{R}_{xx} on the plateau as a function of the magnetic field (see Fig. S15C). The root-mean-square gradually reduces to the noise level above about 5 T.

For a single gate sweep measurement at a fixed field, we only observe a few major oscillations along the width of the plateau. As a result, a given trace may be preferentially weighted positively or negatively. However, when we measure in a range of magnetic fields, we sample over various vortex configurations, and the result is on average neutral. In Fig. S15D we averaged \tilde{R}_{xx} over the gate voltage corresponding to a plateau, and presented $\langle \tilde{R}_{xx} \rangle$ vs. B.

References

- [1] Lee, G.-H. *et al.* Inducing superconducting correlation in quantum Hall edge states. *Nat. Phys.* **13**, 693–698 (2017).
- [2] van Ostaay, J. A. M., Akhmerov, A. R. & Beenakker, C. W. J. Spin-triplet supercurrent carried by quantum Hall edge states through a Josephson junction. *Phys. Rev. B* **83**, 195441 (2011).
- [3] Lian, B., Wang, J. & Zhang, S.-C. Edge-state-induced Andreev oscillation in quantum anomalous Hall insulator-superconductor junctions. *Phys. Rev. B* **93**, 161401 (2016).
- [4] Ihn, T. *Semiconductor Nanostructures* (Oxford University Press, Oxford, 2010).
- [5] Takagaki, Y. Transport properties of semiconductor-superconductor junctions in quantizing magnetic fields. *Phys. Rev. B* **57**, 4009–4016 (1998).
- [6] Akhmerov, A. R. & Beenakker, C. W. J. Detection of valley polarization in graphene by a superconducting contact. *Phys. Rev. Lett.* **98**, 157003 (2007).
- [7] de Gennes, P. G. *Superconductivity of Metals and Alloys* (Perseus Books Publishing, Reading, Massachusetts, 1966).
- [8] Ferry, D. K., Goodnick, S. M. & Bird, J. *Transport in Nanostructures* (Cambridge Univ. Press, Cambridge, UK, 2009).
- [9] Datta, S. *Transport in Mesoscopic Systems* (Cambridge Univ. Press, Cambridge, UK, 1995).
- [10] Groth, C. W., Wimmer, M., Akhmerov, A. R. & Waintal, X. Kwant: A software package for quantum transport. *New J. Phys.* **16**, 063065 (2014).